Journal of Materials Chemistry A

Effect of pore size on heat release from CO_2 adsorption in MIL-101, MOF-177, and UiO-66

Journal:	*Journal of Materials Chemistry A*
Manuscript ID	TA-ART-05-2023-003018.R1
Article Type:	Paper
Date Submitted by the Author:	06-Aug-2023
Complete List of Authors:	Auti, Gunjan; Tokyo Daigaku Kametani, Yuki; Tokyo Daigaku Kimura, Hibiki; Tokyo Daigaku Paul, Soumyadeep; Tokyo Daigaku Hsu, Wei-Lun; Tokyo Daigaku, Mechanical Engineering Kusaka, Shinpei; Nagoya University, Department of Chemistry and Biotechnology, School of Engineering Matsuda, Ryotaro; Nagoya University Uemura, Takashi; The University of Tokyo, Applied Chemistry Chiashi, Shohei; The University of Tokyo, Mechanical Engineering Daiguji, Hirofumi; Tokyo Daigaku, Department of Mechanical Engineering

Journal Name

ARTICLE TYPE

Cite this: DOI: 00.0000/xxxxxxxxxx

Effect of pore size on heat release from CO_2 adsorption in MIL-101, MOF-177, and UiO-66†

Gunjan Auti[a], Yuki Kametani[b], Hibiki Kimura[a], Soumyadeep Paul[a], Wei-Lun Hsu[a], Shinpei Kusaka[c], Ryotaro Matsuda[c], Takashi Uemura[b], Shohei Chiashi[a], and Hirofumi Daiguji*[,a]

Received Date
Accepted Date

DOI: 00.0000/xxxxxxxxxx

Understanding the relationship between the geometry of metal-organic frameworks (MOFs) and the CO_2 enthalpy of adsorption is of utmost importance to control CO_2 adsorption/desorption in MOFs and the associated heat in/out to realize their application in heat pumps and energy storage systems. This study considers the adsorption/desorption characteristics and enthalpy of adsorption of R744 (CO_2) refrigerant on three MOFs (MIL-101, MOF-177, and UiO-66) with decreasing pore sizes using volumetric adsorptions and calorimetric measurements. Grand Canonical Monte Carlo (GCMC) simulations determined the contributions of the interaction energy and configuration of CO_2 adsorbed in the frameworks. Moreover, a confinement parameter (Ψ), defined as the ratio of the Lennard–Jones parameter on the length scale, σ, to the pore size, is introduced using a one-dimensional model for adsorption in MOFs. The results explain the effects of the framework-induced heterogeneity on the adsorbed fluid. At the critical value of Ψ, the formation of potential wells inside the MOF exhibits pitchfork bifurcation. The results indicate a trade-off between the adsorption capacity and enthalpy of adsorption, depending on the parameter Ψ of the MOF. This opens new possibilities for designing MOFs by considering the selection of the central metal atom and the pore radius for the target application.

1 Introduction

Over the past decade, the frequency of extreme heat waves[2] and cold waves[3] has increased drastically due to climate change. This directly impacts the demand for space heating and cooling. According to an International Energy Agency (IEA) survey, the stock of residential air conditioners worldwide is expected to reach up to 3000 million units by 2030.[4] To comply with the Kigali Amendment requirements,[5] the HVAC industry is moving toward natural refrigerants such as CO_2 (R744), ammonia, and water due to their low Global Warming Potential (GWP)[6] and zero Ozone Depletion Potential (ODP).[7] In the vapor compression heat pump (VCHP) cycle, hydrofluorocarbon (HFC)-based refrigerants transport heat through a liquid-vapor phase transition that releases enthalpy of vaporization/condensation (ΔH_{vap}). In a typical VCHP using the R-134a refrigerant, this phase change occurs at a temperature greater than ambient (around 323–343 K) and a pressure of 10–15 bar. However, unlike HFCs, natural refrigerants have low critical temperatures (304.7 K for CO_2, for example). Therefore, it is necessary to operate a conventional vapor compression system with natural refrigerants at transcritical pressures between 75–150 bar to achieve a comparable heat of cooling to ΔH_{vap}. Even though such systems have an excellent coefficient of performance, the ability to operate at lower pressures further enhances both energy efficiency and safety.

A hybrid compression-adsorption heat pump (HCA-HP) cycle is proposed to tackle the problem of high operating pressures.[8] In this cycle (Fig. 1**a** (I)), the refrigerant is compressed to moderately high pressure. It is mixed with a stream of adsorbent particles (1-2), where the high pressure allows adsorbing these particles to release the enthalpy of adsorption (2'-3), which produces the heating effect. These refrigerant-adsorbed particles are then passed through an expansion valve (3-4) to reduce the pressure and cause desorption. As the desorption process is endothermic, it produces a cooling effect by absorbing heat from the surroundings (4-1). This coupled compression-sorption process aids in adsorbent regeneration, reducing the operating pressure to less than 40 bar. However, it is critical to select an appropriate adsorbent based on (i) the enthalpy of adsorption and (ii) the type of adsorption isotherms for the target pressure range and the heating

[a]Department of Mechanical Engineering, The University of Tokyo, 7-3-1 Hongo, Bunkyo-ku, Tokyo 113-8656, Japan. E-mail: daiguji@thml.t.u-tokyo.ac.jp
[b]Department of Applied Chemistry, The University of Tokyo, 7-3-1 Hongo, Bunkyo-ku, Tokyo 113-8656, Japan.
[c]Department of Materials Chemistry, Nagoya University, Furo-cho, Chikusa-ku, Nagoya 464-8603, Japan.

† Electronic Supplementary Information (ESI[1]) available: [Supporting information including the x-Ray diffraction patterns for the MOF samples, Lennard-Jones potentials used in the GCMC simulation, and the GCMC scheme is included (PDF)]. See DOI: 00.0000/00000000.

capacity of the HCA-HP cycle.

Metal-organic frameworks (MOFs) are highly porous crystalline structures comprising metal nodes and organic linkers that are excellent adsorbents due to their mesoporous structure. Additionally, altering their structure and central metal atoms allows tailoring to different applications,[9] making MOFs up-and-coming candidates for HCA-HP adsorbents.[8,10–13] Further, MOFs have been developed for a wide range of applications from gas storage and separation,[14–20] heterogeneous catalysis,[21,22] drug delivery,[23] sensors,[24] and desalination,[25] due to their tunability and large surface area.

Generally, MOFs have been created to keep the adsorption capacity as the main focus; hence, MOFs with very large Brunauer–Emmett–Teller (BET) surface areas have been developed by altering structure topologies and pore sizes.[26,27] However, the enthalpy of adsorption must be maximized to provide the HCA-HP cycle with a high heating/cooling capacity. In addition, a step-shape adsorption isotherm is required to minimize the compression work (low-pressure ratio) and for easy regeneration (swift desorption by reducing the pressure). With ever-stringent environmental regulations, it is imperative to explore materials that show a higher cumulative enthalpy of adsorption as well as a step-shaped adsorption isotherm. This fundamental study underscores the need for this research direction and proposes a theoretical framework to classify MOF materials from a high COP heat pump point of view.

This work focuses on CO_2 as a natural refrigerant due to its low toxicity and abundant availability. Therefore, understanding the structural, dynamic, and thermodynamic properties of CO_2 in MOFs is the first step in developing a suitable class of MOFs for HCA-HP cycles. Moreover, several studies have suggested polymorphic phase transitions of CO_2 under confinement and high pressure.[28–34] This begs the question of whether CO_2 adsorbed in MOF mesopores exhibits the same properties as the polymorphic transition. If so, a further question arises as to whether it depends on the pore size and how this affects the enthalpy of adsorption. The current study investigates the equilibrium thermodynamic characteristics of adsorbed CO_2 by employing the Grand Canonical Monte Carlo (GCMC) method. An alternative viewpoint is introduced to comprehend the adsorption phenomena within mesopores, emphasizing the formation of potential wells. The findings reveal a distinct bifurcation in the shapes of these wells, influenced by the interplay of van der Waals and coulombic interactions, specifically in relation to the heterogeneity-to-cavity size ratio.

This is achieved by exploring the CO_2 adsorption properties of different MOFs (UiO-66, UiO-67, UiO-68, MOF-177, MOF-5, PCN-221 and MIL-101(Cr)) to investigate the impact of varying the pore sizes. These MOFs exhibit pore diameters ranging from 0.6-3.4 nm. Out of these, MIL-101(Cr), MOF-177, and UiO-66 are studied experimentally to validate the results of GCMC simulations. Note that MIL-101 has three different pores, and this study focuses primarily on the largest of the three (see Fig. 1**b**). The 'Type IV' adsorption isotherm with a rapid increase in adsorption is characteristic of MIL-101. A schematic of the HCA-HP cycle designed with MIL-101 as the adsorbent is shown in Fig. 1**a** (I, II, III). The adsorption isotherm and the enthalpy of adsorption are obtained from the Grand Canonical Monte Carlo (GCMC) simulations and are validated using experimental techniques. Moreover, the simulations explain the pore-filling process, the differential enthalpy of adsorption, and the interactions between MOFs and CO_2, as shown in Fig. 1**b**, Fig. 1**c**, Fig. 1**d**. Our results indicate that the differential enthalpy of adsorption has various trends for the different pore diameters. Fig. 1**c** illustrates the enthalpy of adsorption trend for MIL-101, which decreases at lower loadings ($N/N_{max} < 0.2$) and increases at higher loadings ($N/N_{max} > 0.8$). These variations in the differential enthalpy of adsorption are explained by forming potential wells inside the MOF nanopores. Moreover, the contributions of van der Waals and Coulombic interactions are studied by comparing the energy released due to each interaction, as shown in Fig. 1**d**. Further, the radial distribution functions obtained from the GCMC simulations demonstrate that for MIL-101 and MOF-177, the CO_2-CO_2 radial distribution function (RDF) resembles the bulk liquid phase. On the other hand, UiO-66 resembles the solid bulk phase.

This paper is organized as follows. Section 2 details the experimental and numerical methods to obtain the adsorption isotherms and enthalpy of adsorption. Section 3 presents the structure and geometry of the pores, adsorption isotherms, and enthalpy of adsorption obtained from experimental methods and the GCMC simulations. Section 4 qualitatively discusses the causality of the obtained results through interaction energies and RDFs. The nature of adsorbed fluid at different pore radii is also discussed based solely on the resemblance of the RDFs to bulk phases. This section also introduces a one-dimensional model for adsorption and a confinement parameter (Ψ) to capture the quantitative impact of the pore size. Section 5 presents general conclusions and makes suggestions suitable for HCP-HP cycles.

2 Methods

2.1 Experimental Methods

2.1.1 Material Synthesis and Characterization

The MIL-101, MOF-177, and UiO-66 samples were synthesized using methods found in the literature. The synthesis of MIL-101 is given as follows: Chromium (III) nitrate $Cr(NO_3)_3{\cdot}9H_2O$ (400 mg, 1.00 mmol), 1.00 mmol of fluorohydric acid, 1,4-benzene dicarboxylic acid, and H_2BDC (164 mg, 1.00 mmol) were mixed in 4.8 mL H_2O (265 mmol) in a glass container. The mixture was then introduced in a hydrothermal bomb and placed in an autoclave at 493 K for 8 h. The mixture was first filtered using a large pore-fritted glass filter to eliminate most of the carboxylic acid. Then, the free terephthalic acid was eliminated, and the MIL-101 powder was separated from the solution using a small pore paper filter.[35]

To synthesize MOF-177, 1,3,5-Tris(4-carboxyphenyl)benzene (0.597 g, 1.36 mmol) and $Zn(NO_3)_2{\cdot}4H_2O$ (2.869 g, 11.0 mmol) were dissolved N,N-diethylformamide (DEF, 150 mL) in a glass bottle. The solution was heated in an oven at 358 K for 70 h. After cooling to room temperature, the resultant crystals were washed with anhydrous DMF (3 × 50 mL) for 3 h and anhydrous chloroform (2 × 50 mL) for 2 days. The obtained colorless MOF-177

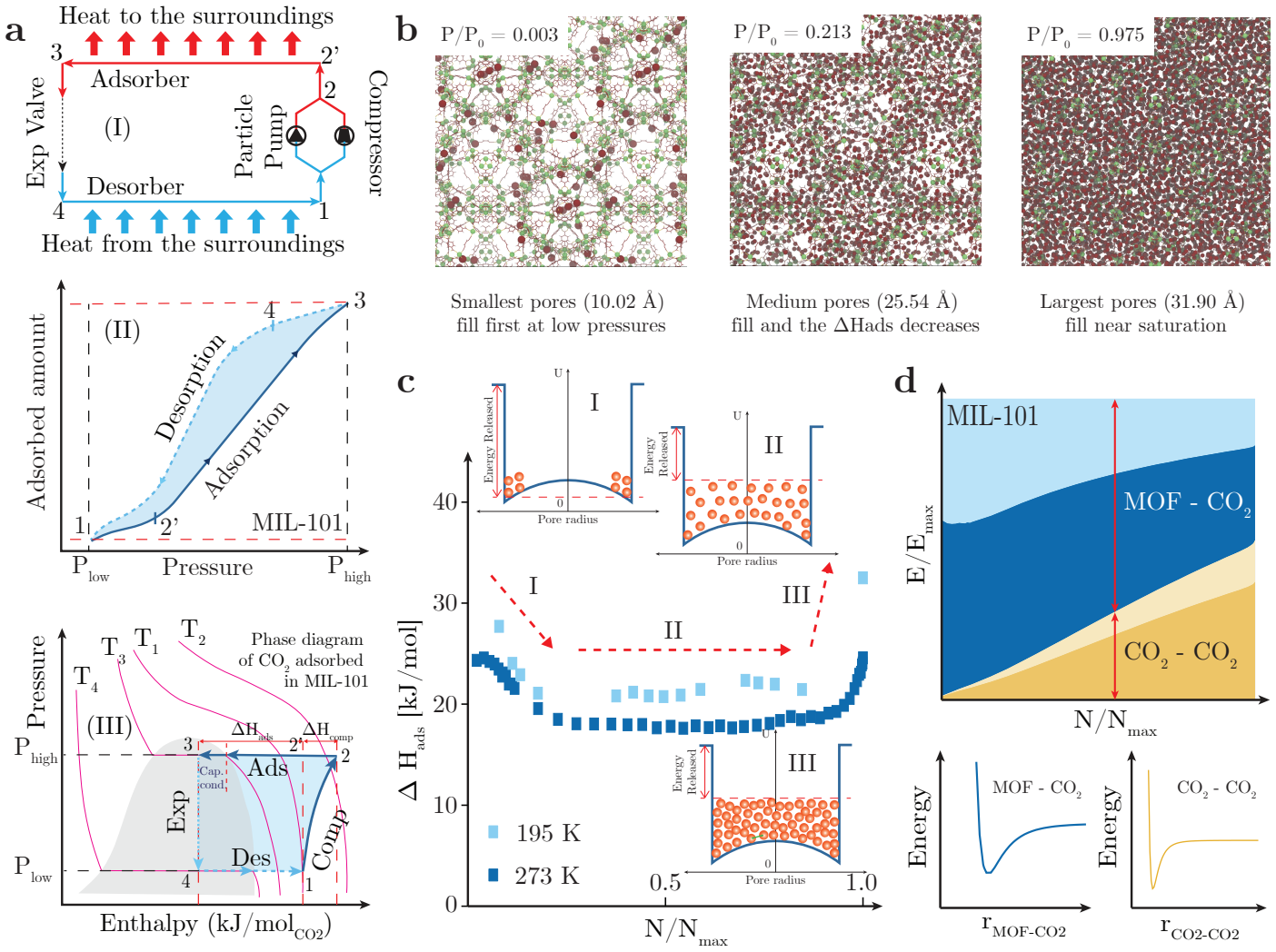

Fig. 1 Adsorption process for MIL-101

a(I) The proposed HCA-HP cycle. The 1-2' is isentropic compression, 2'-3 is the high-temperature adsorption, 3-4 is isenthalpic expansion, and 4-1 is the low-temperature desorption. (II) The CO_2 adsorption cycle for the proposed HCA-HP cycle. (III) The p-H diagram for the HCA-HP cycle is plotted as a schematic phase diagram of the adsorbed CO_2 in MIL-101. b Pore-filling process of MIL-101 at 273 K obtained using GCMC simulations. The order of pore filling is from smallest to largest, with the largest near the saturation pressure of bulk CO_2 (34.85 bar). c Differential enthalpy of adsorption (ΔH_{ads}) with respect to loading. During the initial pore-filling process (I), ΔH_{ads} decreases as the adsorption site are further from the metal atom, and the depth of the potential well is less. In region (II), ΔH_{ads} is constant during medium pore-filling. Near saturation, the differential enthalpy of adsorption increases (III) due to the capillary condensation in the nanopore of MIL-101. d Partition of interaction energy released due to the van der Waals and Coulombic interactions between the MOF-CO_2 and CO_2-CO_2 interactions as obtained from GCMC simulations.

crystals were dried under vacuum at room temperature.[36]

To synthesize UiO-66, $ZrCl_4$ (0.242 g, 1 mmol) was dissolved in DMF (60 mL) in a round-bottom flask. To the solution, acetic acid (1.72 mL, 30 mmol), and terephthalic acid (0.174 g, 1 mmol) were added and stirred at room temperature until dissolved. While stirring, the solution was heated in an oil bath at 393 K for 24 h. After cooling to room temperature, the resultant solid was centrifuged and washed with methanol. The obtained white powder of UiO-66 was dried under vacuum at 423 K overnight.[37]

The structural characterization of the synthesized MOFs was performed on an X-ray powder diffractometer (XRD, SmartLab 3 kW, Rigaku). Nitrogen adsorption and desorption measurements were performed using a surface area and pore size distribution analyzer (BELSORP MAX II, MircotracMRB) at 77 K up to the saturation pressure (1 atm). The specific surface area was calculated using the BET method,[38] and the pore size distribution was obtained using non-local density functional theory (NLDFT). The obtained XRD images and nitrogen isotherms for all MOFs are included in the ESI[1] Section S1.

2.1.2 Volumetric Adsorption

Fresh samples of UiO-66, MOF-177, and MIL-101(Cr) were degassed under vacuum at 383 K for 12 h. The pretreated MOF sample was attached to the surface area and pore size distribution analyzer, as shown in Fig. 2**a**. The CO_2 was introduced to the setup at regular pressure intervals, and its adsorbed volume was measured. The sample was maintained at 195 K (sublimation temperature of CO_2 at atmospheric pressure) throughout the ex-

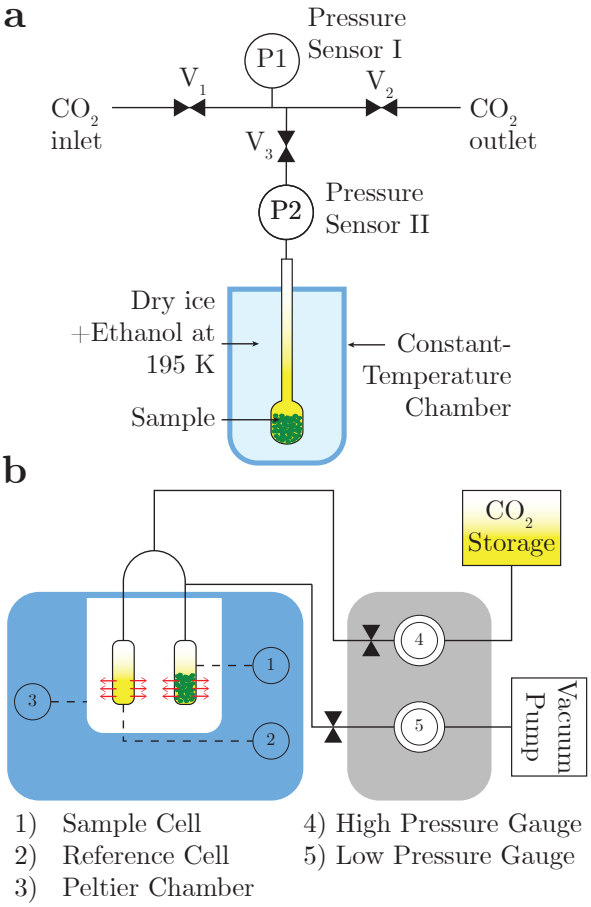

Fig. 2 Experimental setup
Schematic diagrams for a the nitrogen adsorption and desorption measurement system (BELSORP MAX II, MicrotracMRB) and b the Calvet-type calorimeter (Microcalvet Ultra, Setaram) with a customized gas pressure control system.

periment using a dry ice and ethanol mixture. This temperature was chosen due to the 1 atm pressure limitation of the equipment, as saturation can be achieved only at this temperature.

2.1.3 Enthalpy Measurements

The CO_2 heat of adsorption measurement was performed using a Calvet-type calorimeter (Microcalvet Ultra, Setaram) with a customized gas pressure control system. The MOF samples were placed in a steel sample cell pretreated to 383 K under vacuum before the measurements. The sample and reference cells were connected to a pressure control system, as shown in Fig. 2**b**. The CO_2 was introduced to the sample and reference cells at regular pressure intervals. At each pressure, the heat flow was measured with respect to time until equilibrium was reached. The heat of adsorption at a step change in pressure was obtained by integrating over the heat flow vs. time curve. The experiments were performed at 273 K. The heat flow curves are shown in the ESI[1] Section S2.

2.2 Grand Canonical Monte-Carlo Simulations

The enthalpy of adsorption releases due to the CO_2-MOF and CO_2-CO_2 interactions. Raman spectroscopy of the CO_2 adsorbed in MOF is among the most intuitive methods to observe the interactions of CO_2 molecules adsorbed in the MOF.[39] However, limitations in this approach and the difficulty of constructing a gas cell do not always make this available. On the other hand, molecular simulations are a powerful tool and provide significant useful information. Here, the equilibrium thermodynamic properties of CO_2 adsorption in MOFs were obtained from the GCMC simulations and compared to the available literature data and to the experiments performed in this paper.

The GCMC simulations were performed using the RASPA[40] simulation software package. All simulations include a 100,000-cycle equilibration period and a 500,000-cycle production run. The structure of all the frameworks is rigid; all framework atoms are held fixed at their crystallographic positions. The transferable potentials for the phase equilibria (TraPPE)[41] model with a rigid structure were used for the CO_2 as they predict the solid-fluid-gas phase equilibrium with considerable confidence.[42] The CO_2 molecules can undergo three different types of GCMC motion: translation, rotation, and swap. The CO_2-MOF and CO_2-CO_2 interactions are modeled using the Lennard–Jones (L–J) and Coulombic potential functions. The universal force field (UFF)[43] defines the L–J parameters for each framework atom of the MOF. Lorentz–Berthelot mixing rules were applied to model the CO_2-MOF interactions. The charge distribution was calculated using the charge equilibration method given by Wilmer and Snurr.[44] The L–J cut-off distance of 12.5 Å was used, while the Ewald method was employed with a precision of 1e-06. All parameters are summarized in Sec. S3 of the ESI[1].

The differential enthalpy of adsorption is defined as the difference in the internal energy of one CO_2 molecule inside and outside the framework.[45–47] That is,

$$\Delta H = \langle U_{hg} \rangle - \langle U_h \rangle - \langle U_g \rangle - k_B T \quad (1)$$

where $\langle U_{hg} \rangle$, $\langle U_h \rangle$, and $\langle U_g \rangle$ are the average energies of the CO_2 molecule (guest) inside the MOF (host), average structural energy of the MOF framework (host), and average structural energy of a single CO_2 molecule (guest) in the gas phase, respectively. The $k_B T$ term accounts for the pV work necessary to push the CO_2 molecule into the ideal bulk phase during desorption. As the TraPPE model with rigid CO_2 is used, $\langle U_g \rangle$ is zero. Moreover, the framework is considered rigid, implying $\langle U_h \rangle$ is also zero.

The GCMC simulations conducted in this study allow for an analysis of the contributions of various interactions to the overall potential energy. Specifically, the energy budget focuses on comparing the contributions of different interactions, namely Framework-CO_2 van der Waals (vdW), Framework-CO_2 Coulombic, CO_2-CO_2 vdW, and CO_2-CO_2 Coulombic interactions. This analysis provides insights into the relative importance of these interactions in the adsorption process. Furthermore, to gain a better understanding of the distribution of CO_2 within the MOF cavity, two types of radial distribution functions (RDFs) are examined. The first type investigates the distribution of CO_2 molecules around other CO_2 molecules, shedding light on the spatial arrangement and clustering behavior of CO_2 molecules within the MOF. The second type focuses on the distribution of

CO_2 molecules around the central metal atom, providing insights into the coordination and spatial proximity between CO_2 and the metal sites in the MOF structure. RDFs are calculated according to the following formulation:

$$g(r) = \frac{N(r, r+dr)}{4\pi r^2 n dr} \quad (2)$$

Here, r is the radial coordinate assuming the carbon of CO_2 or the central metal atom as the origin, dr is the bin width, and N is the number of particles in the bin. n is the normalization factor, which is the average number density throughout the cavity. The bin width is considered 0.0125 for calculating all the radial distribution functions in the current work.

3 Results

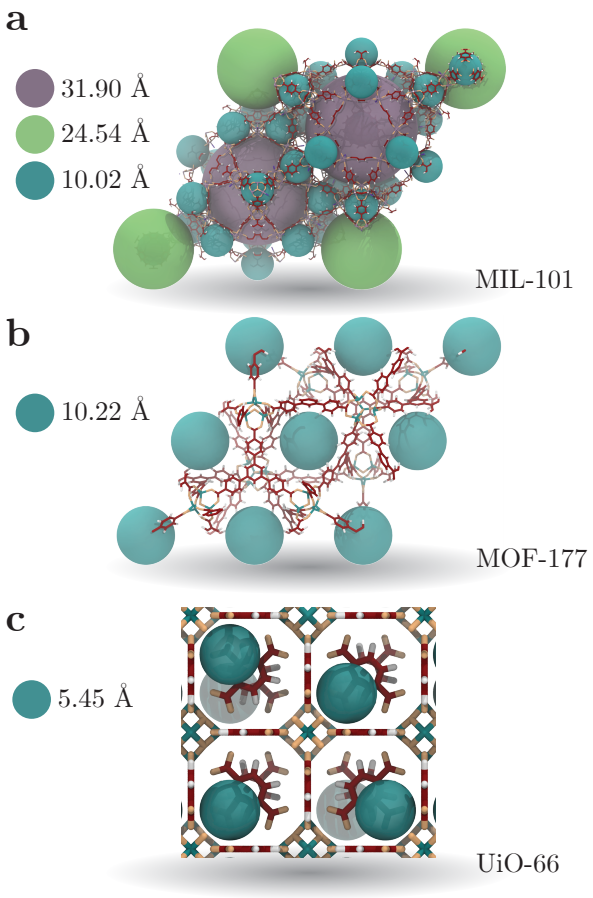

Fig. 3 Pore size distribution
Artistic view of pore the sizes and positions obtained from non-local density functional theory (NLDFT) for a MIL-101, b MOF-177, and c UiO-66.

3.1 Structure and Geometry of MOFs

Three MOFs (MIL-101, MOF-177, and UiO-66) were chosen based on diversity in their pore radii. The pore size distribution (PSD) is obtained via NLDFT using the experimentally obtained N_2 adsorption isotherm at 77 K, as shown in Fig. 3. Note that the crystal structures (.cif files) of the three MOFs shown in Fig. 3 (position data and charge distribution) were obtained from the Cambridge Crystallographic Data Centre (CCDC) database. The experimentally obtained pore diameters are shown in the appropriate positions.

The MIL-101 has three pore sizes: small (super tetrahedron (ST), blue spheres in Fig. 3**a**) at 10 Å, medium (green spheres in Fig. 3**a**) at 25 Å, and large (purple spheres in Fig. 3**a**) at 32 Å. The Cr_3O trimers occupy the vertices of the ST, and the edges are occupied by 1,4-benzene dicarboxylate (BDC). The large and medium pores (shown in purple and green, respectively) are encapsulated within a polyhedron and assembled by the corner-sharing ST. The MOF-177 has a single cavity (blue spheres in Fig. 3**b**) at 10 Å surrounded by a diamond-shaped structure of 1,3,5-benzenetribenzonate (BTB) linkers around the Zn_4O octahedral units. Moreover, the UiO-66 structure has cuboctahedral units consisting of ZrO_4 at each vertex and 1,4-benzene dicarboxylic acid (BDC) connecting the edges of the structure. This forms a single cavity of around 6 Å, as shown in Fig. 3**c** (blue spheres).

3.2 Adsorption Isotherms

The MIL-101, MOF-177, and UiO-66 exhibit different adsorption isotherms based on their pore radii and are labeled Type IV, Type V, and Type I, respectively. For MIL-101 with a multi-pore structure, the IUPAC Type IV adsorption isotherm with a step-like shape is observed. At 195 K, Type IV behavior is seen (Fig. 4**a**) with a step-wise increase around $P/P_{sat} \approx 0.5$. The small and medium cavities gradually fill at lower pressures ($P/P_{sat} < 0.3$), while the large cavities suddenly fill at a relative pressure within 0.3–0.5 (Fig. S16 of the ESI[1]).

The MOF-177 has a Type V isotherm, which shows a continuous increase for lower pressures and a sharp increase for higher pressures with eventual saturation. The adsorption monotonically increases for $P/P_{sat} < 0.1$ and sharply increases at $P/P_{sat} \approx 0.1$ (Fig. 4**c**). The UiO-66 has a typical Type I adsorption isotherm at 195 K (Fig. 4**e**). The N_{max} plateau is attained at $P/P_{sat} \approx 0.2$.

The shapes of adsorption isotherms obtained from experiments and the GCMC simulation agree with each other validating the GCMC simulations at 195 K. Additional Experimental data for adsorption isotherms at 195 K and 205 K is provided in the Fig. S13 of the ESI[1]

3.3 Enthalpy of Adsorption

The cumulative enthalpy of adsorption is shown in Fig. 4**b**, Fig. 4**d**, and Fig. 4**f**. The solid triangles in each of these figures represent the experimentally obtained values and the crosses represent the values obtained from the GCMC simulation. From the figure, it can be observed that GCMC simulations are in excellent agreement with the experimental values at 273 K.

For MIL-101 (Fig. 5**a**), the differential enthalpy of adsorption (ΔH_{ads}) decreases with the amount of CO_2 adsorbed at lower values of N/N_{max} (<0.2, section I in Fig. 5**a**). Near saturation, the differential enthalpy of adsorption starts to increase again (N/N_{max}<0.2, section III in Fig. 5**a**). The differential enthalpy of adsorption does not change in section II of Fig. 5**a** (0.2<

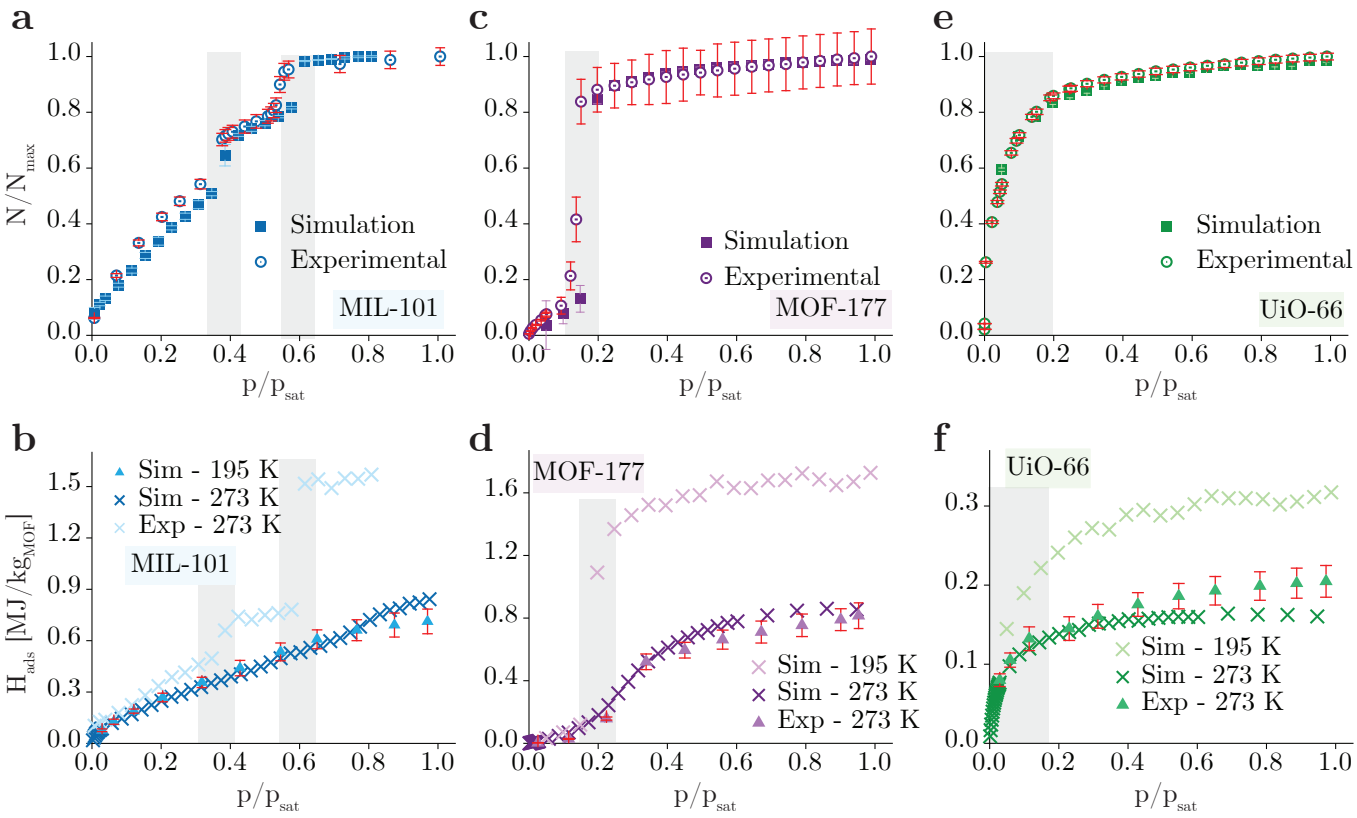

Fig. 4 Validation of GCMC simulations
MIL-101: a Adsorption isotherm obtained experimentally (hollow circles) and through GCMC simulations (solid squares) at 195 K (P_{sat} = 1.01 bar). The grey-shaded region highlights the step-wise increase during loading. b The cumulative enthalpy of adsorption obtained from GCMC simulation at 195 K (light blue crosses), 273 K (cobalt blue crosses), and experimentally at 273 K (cobalt blue triangles). Steps similar to adsorption isotherms are seen in the cumulative enthalpy. MOF-177: Similar to the MIL-101 case, c is the adsorption isotherm with the grey-shaded region highlighting the step-wise increase. d Cumulative enthalpy of adsorption at 195 K (lilac crosses), 273 K (purple crosses) obtained from GCMC simulations, and 273 K (purple triangles) obtained experimentally. UiO-66: e Adsorption isotherm at 195 K where the shaded region highlights the exponential increase in the adsorption. f Cumulative enthalpy of adsorption at 195 K (lawn green crosses), 273 K (forest green crosses) obtained through GCMC simulations, and 273 K (forest green triangles) obtained experimentally.

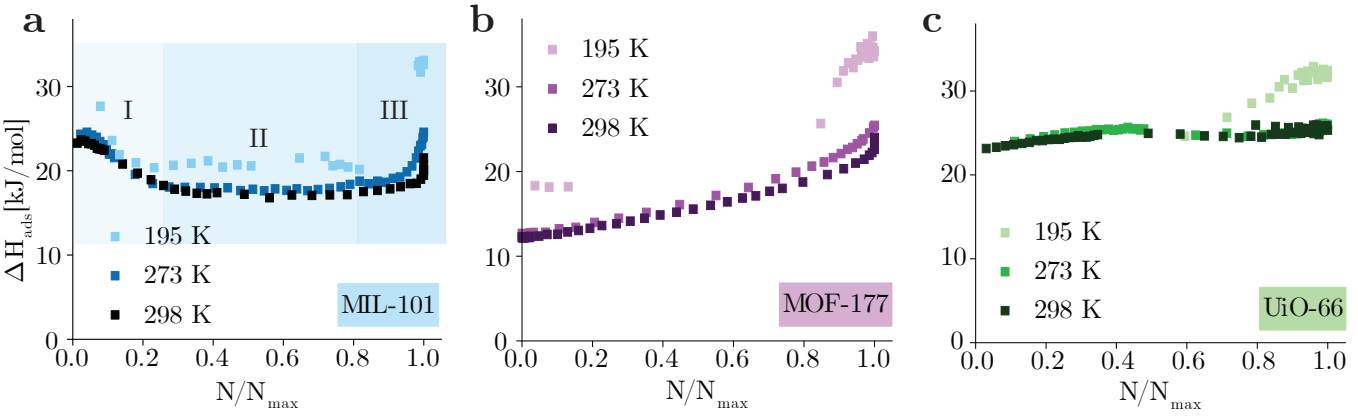

Fig. 5 Differential enthalpy of adsorption (GCMC Simulations)
MIL-101: a In section I ($0 < N/N_{max} < 0.2$), a decreasing trend is observed. In section II ($0.2 \leq N/N_{max} < 0.8$), ΔH_{ads} remains constant. An increasing trend is observed in section III ($N/N_{max} \geq 0.8$). MOF-177: b Differential enthalpy of adsorption at 195 K (lilac squares), 273 K (purple squares), and 298 K (violet squares) shows an increasing trend throughout the pressure range. UiO-66: Differential enthalpy of adsorption at 195 K (lawn green squares), 273 K (forest green squares), and 298 K (dark green squares).

$N/N_{max} < 0.8$). For MOF-177 with a pore size of 10.22 Å, (Fig. 4e), ΔH_{ads} increases with respect to the amount adsorbed. For UiO-66

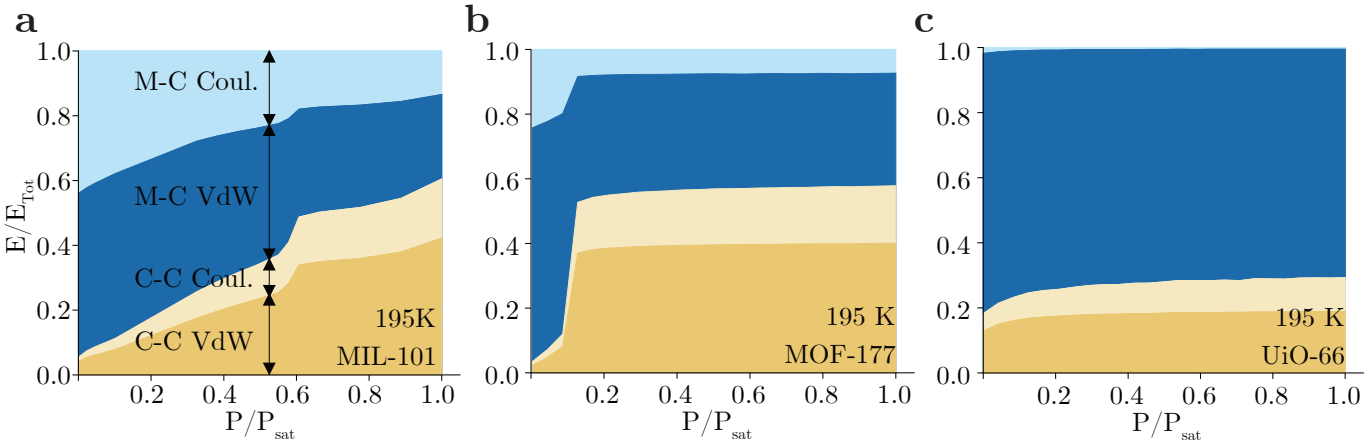

Fig. 6 Interaction Energy Budget
The relative contributions of interaction energies with respect to P/P_{sat}. The light blue region is the Framework-CO_2 Coulombic interactions, the dark blue region is the MIL-101-CO_2 van-der Waals interaction, the light yellow region is the CO_2-CO_2 Coulombic interaction, and the ochre yellow region is the CO_2-CO_2 van-der Waals interaction. a MIL-101, b MOF-177, and c UiO-66

(Fig. 4**h**), the differential enthalpy remains around 24–25 kJ/mol throughout the N/N_{max} range. The trends of the differential enthalpy of adsorption are similar at 195 and 273 K (Figs. 5**a**, 5**b**, and 5**c**), implying that the differential enthalpies of adsorption are independent of temperature, as found by Cao et al.[48]

4 Discussion

4.1 Energy Budget and Radial Distribution Functions

During adsorption, randomly moving high-energy molecules in the bulk phase interact with the adsorbent and find a lower energy state (potential well) due to the van der Waals and Coulombic interactions. The difference between their initial energy and the final steady-state energy is released as the enthalpy of adsorption. The amount of energy released depends on the strength of the attractive forces between the adsorbent and adsorbate (depth of potential well). In this case, the interactions include the MOF and CO_2 molecules and the inter-molecular interactions between adsorbed CO_2.

To understand the trends of the adsorption isotherms and differential enthalpy of adsorption interaction energies released due to the van der Waals and Coulombic interactions are plotted in the interaction energy budget diagrams (Fig. 6). The major contributing factors for these interactions are the MOF-CO_2 Coulombic interaction ((M-C Coul.) sky blue regions in Fig. 6), the MOF-CO_2 van der Waals interaction ((M-C VdW) cobalt blue regions in Fig. 6), the CO_2-CO_2 Coulombic interaction ((C-C Coul.) light yellow regions in Fig. 6), and the CO_2-CO_2 van der Waals ((C-C VdW) ochre yellow regions in Fig. 6) interaction. As these forces depend significantly on the inter-molecular distance, the RDFs for metal-CO_2 and CO_2-CO_2 are also analyzed (Fig. 7). The energy budget and RDFs are described for MIL-101, MOF-177, and UiO-66.

The MIL-101 exhibits a typical Type IV adsorption isotherm (Fig. 4**a**) with a step-wise increase in loading at $P/P_{sat} \approx 0.5$. The differential enthalpy of adsorption (Fig. 5**a**) displays a decreasing and increasing trend at lower and higher loadings, respectively. At lower pressures ($P/P_{sat} < 0.2$), the MIL-101-CO_2 interaction dominates, as seen in Fig. 6**a**. The MIL-101-CO_2 interaction energy (M-C Coul. and M-C VdW regions in Fig. 6**a**) decreases with the pressure. This indicates that adsorbed CO_2 molecules interact with only one metal site, and there are limited CO_2-CO_2 interactions. With further loading, CO_2 is adsorbed from the Cr metal atom and weakens the interactions with MIL-101, which explains the decreasing trend in the differential enthalpy at lower pressures. As the pressure further increases, the number of adsorbed CO_2 molecules increases (Fig. S16 in the ESI[1]). The energy is released due to increases in the inter CO_2 interactions (light and dark yellow regions). The sudden change near $P/P_{sat} \approx 0.5$ corresponds to the step in the adsorption isotherm (the grey-shaded region in Fig. 4**a**) due to capillary condensation.[49] Below the saturation pressure, the differential enthalpy of adsorption increases rapidly as the CO_2-CO_2 interactions increase due to greater space density. The increasing trend in the differential enthalpy of adsorption corresponds to this capillary condensation. It is noted that the sudden increase in the differential enthalpy of adsorption does not occur when the small and medium pores are completely filled (Fig. 1**b** at 273 K), suggesting that there is a minimum pore radius beyond which the sudden increase in differential enthalpy of adsorption occurs.

The GCMC simulations show that the three pores in the MIL-101 fill in ascending order, as illustrated in Fig. S16 in the ESI.[1] The same is observed from the RDFs for CO_2 molecules around Cr atoms in MIL-101 (Fig. 7**a**). At lower pressures (P/Psat = 0.1 in Fig. 7**a**), the majority of the adsorption occurs near the metal site (peak I). As the pressure increases, the metal site remains one of the adsorption sites, while the remaining adsorbed CO_2 is distributed uniformly around the medium and large cavities. In Fig. 7**b**, for $P/P_{sat} \geq 0.5$ (Fig. 7**b**), the RDF for CO_2 around CO_2 resembles the bulk liquid phase, and as the pressure continues to increase, the RDF starts resembling the bulk liquid phase and demonstrates the hypothesized capillary condensation earlier.

The adsorption isotherm for MOF-177 shows IUPAC Type V be-

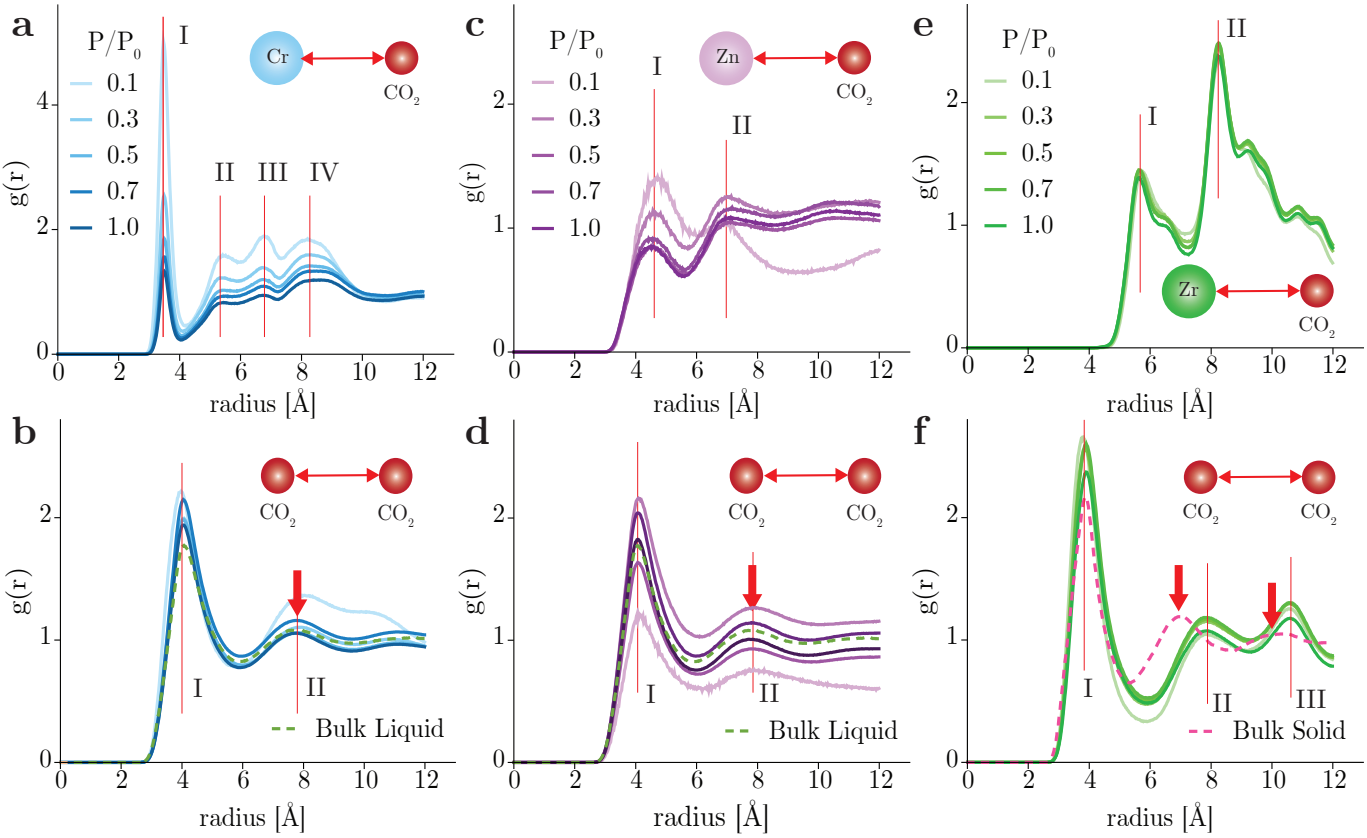

Fig. 7 Radial Distribution Functions
Radial distribution functions (RDFs) of CO_2 around central metal atoms are shown in a CO_2-Cr (MIL-101), c CO_2-Zn (MOF-177), and e CO_2-Zr (UiO-66).
RDFs of the CO_2 around CO_2 at 273 K for b MIL-101, d MOF-177, and f UiO-66. The dashed lines illustrate the RDFs for the bulk solid and bulk liquid phases of the CO_2.

haviors with a step-wise increase in the adsorption with respect to pressure (the grey-shaded region in Fig. 4**c**). The differential enthalpy of adsorption exhibits a peculiar monotonically increasing trend (Fig. 5**b**). At lower pressures ($P/P_{sat} < 0.1$), the CO_2-CO_2 interactions are negligible compared to MOF-177-CO_2 interactions (Fig. 6**b**). The step-wise increase near $P/P_{sat} \approx 0.1$ corresponds to capillary condensation, as seen in Fig. 4**c**. The lower relative pressure for capillary condensation compared to MIL-101 ($P/P_{sat} \approx 0.5$) is attributed to the greater degree of confinement, which increases the CO_2-CO_2 interactions due to the smaller pore size of MOF-177.

The radial distribution of CO_2 molecules around the Zn metal atom indicates that at lower pressures ($P/P_{sat} = 0.1$ in Fig. 7**c**), the primary adsorption site is closer to the metal atom. This is because most of the adsorbed CO_2 is in the first coordination sphere around the Zn metal site (Peak I in Fig. 7**c**). As the pressure increases, the adsorption site moves away from the metal atom and toward the center of the pore (Peak II in Fig. 7**c**). Near saturation, the adsorbed CO_2 molecules are evenly distributed throughout the pore. Furthermore, the RDF for CO_2 around CO_2 (Fig. 7**d**) resembles the bulk liquid phase for $P/P_{sat} \geq 0.3$, which maintains the hypothesis of capillary condensation associated with the step-shaped adsorption isotherm.

The differential enthalpy of adsorption is nearly constant throughout the entire loading range. The UiO-66 adsorption isotherm is a typical Type I adsorption isotherm with a loading plateau that reaches saturation around $P/P_{sat} = 0.2$. The pore diameter is around 6 Å, and one CO_2 molecule is 3.32 Å in diameter. This means a single pore can accommodate a maximum of 7 CO_2 molecules, even considering complete packing and zero intermolecular spacing between adsorbed molecules. The narrow pore size implies they cannot accommodate more than a single layer of CO_2 molecules, as shown in the pore-filling diagram (Fig. S16) in the ESI.[1] This monolayer formation does not allow the possibility of capillary condensation.[50] Additionally, Fig. 6**c** illustrates that the UiO-66-CO_2 interactions dominate throughout the pressure range, implying there is no capillary condensation. However, as seen in previous sections, the differential enthalpy of adsorption is more than the MIL-101 and MOF-177. This means that each adsorbed CO_2 interacts with Zr atoms beyond the adsorbing unit cell (the nearest Zr atom and those in adjacent cells), releasing more energy due to the smaller pore size.

This process can be better illustrated through Fig. 7**e**, where peak II is higher than peak I for the entire pressure range, indicating that the center of the pore ($\sim$ 8Å) is the primary adsorption site rather than close to the Zr metal atom, which allows it to interact with more ZrO_4 units. As opposed to the earlier cases, in the case of UiO-66, the RDF for the adsorbed CO_2 (Fig. 7**f**) has 3

distinct peaks which resemble the RDF of a *bulk solid* phase. This can be explained due to the higher degree of confinement and the overlapping coordination spheres of two or more Zr atoms. The pores in UiO-66 completely fill up, even at relatively low pressures to produce a solid-like RDF.

However, there is a question regarding the factors that contribute to the observed variations in the adsorption isotherms among the selected MOFs, including differences in charge distribution, pore structures, and cavity shapes. In order to eliminate the effect of these factors, an additional analysis was conducted using UiO-66, UiO-67, and UiO-68, and the results are presented in Section S4 of the ESI[1]. The trends observed in the UiO family of MOFs are consistent with the discussion presented earlier, highlighting the dominant influence of pore size on the adsorption process compared to other parameters. This further reinforces the significance of pore size in determining the behavior of the adsorption process.

Nevertheless, in order to achieve a comprehensive understanding of the adsorption process, it is imperative to investigate the non-equilibrium adsorption-desorption process. This necessitates the utilization of molecular dynamics simulations to study the dynamic behavior of the adsorbed fluid[51,52], which would require a separate study.

4.2 Pore Confinement Parameter

A straightforward one-dimensional model of a MOF consisting of only metal atoms and van der Waals interactions is proposed to simplify and summarize the numerical results. The unit cell is considered between positions (-a,0) and (a,0), and adsorption occurs only along the axis joining the metal atoms, as shown in Fig. 8**a**. Let the L–J parameters for the metal atom be σ_m and ε_m and for the CO_2 molecule be σ_{co2} and ε_{co2}. Then, using the Lorentz–Berthelot mixing rules gives,

$$\sigma_{mc} = \frac{\sigma_m + \sigma_{co2}}{2} \quad \text{and} \quad \varepsilon_{mc} = \sqrt{\varepsilon_m \varepsilon_{co2}} \tag{3}$$

Here the coarse-grained model of CO_2 is used to define the values of L–J parameters[53]. In addition, the charge on the metal atom is $+Q$. The charge distribution of the CO_2 molecule is the same as the TraPPE model as listed in the ESI[1]. Using these values for L–J parameters and charge distribution, the potential energy for a system at infinite dilution is written as:

$$\begin{aligned} U(r) = {} & \frac{-\mu Q}{4\pi\varepsilon_0}\left[\frac{1}{(a-r)((a-r)^2-d^2)} + \frac{1}{(a+r)((a+r)^2-d^2)}\right] \\ & + 4\varepsilon_{mc}\left[\left(\frac{\sigma_{mc}}{a+r}\right)^{12} - \left(\frac{\sigma_{mc}}{a+r}\right)^{6}\right] \\ & + 4\varepsilon_{mc}\left[\left(\frac{\sigma_{mc}}{a-r}\right)^{12} - \left(\frac{\sigma_{mc}}{a-r}\right)^{6}\right] + \ldots \end{aligned} \tag{4}$$

where, d is the C=O bond length and $\mu = 2qd^2$ is the quadrupole moment of CO_2. In Eq. 4, a dimensionless distance coordinate is defined as $x = r/a$. In the resulting equation, $d^2/a^2 << 1$ is ignored and the remaining equation is differentiated with respect to x and equated with zero to find the local equilibria along the axis joining the centers of the metal atoms.

$$\begin{aligned} \frac{\partial U}{\partial x} = {} & \frac{1}{4\varepsilon_{mc}}\left[\frac{1}{(1+x)^4} - \frac{1}{(1-x)^4}\right] \\ & + \frac{8\pi\varepsilon_0 a^3}{\mu Q}\left[\frac{-12\sigma_{mc}^{12}}{(1+x)^{13}} + \frac{6\sigma_{mc}^{6}}{(1+x)^{7}} + \frac{12\sigma_{mc}^{12}}{(1-x)^{13}} + \frac{-6\sigma_{mc}^{6}}{(1-x)^{7}}\right] = 0 \end{aligned} \tag{5}$$

In Eq. 5, we can define $\Psi = \sigma_{mc}/a$ as the confinement parameter. In Eq. 5, $x = 0$ is one of the roots as the forces are balanced at $x = 0$, making it an equilibrium point. Moreover, if there are additional equilibrium positions in the one-dimensional pore, the polynomial must have roots in the interval (-1,1). Considering the symmetric nature (around $x = 0$) of the problem, if one of the roots is $\sqrt{\tilde{c}}$, the other has to be $-\sqrt{\tilde{c}}$. Therefore, the polynomial

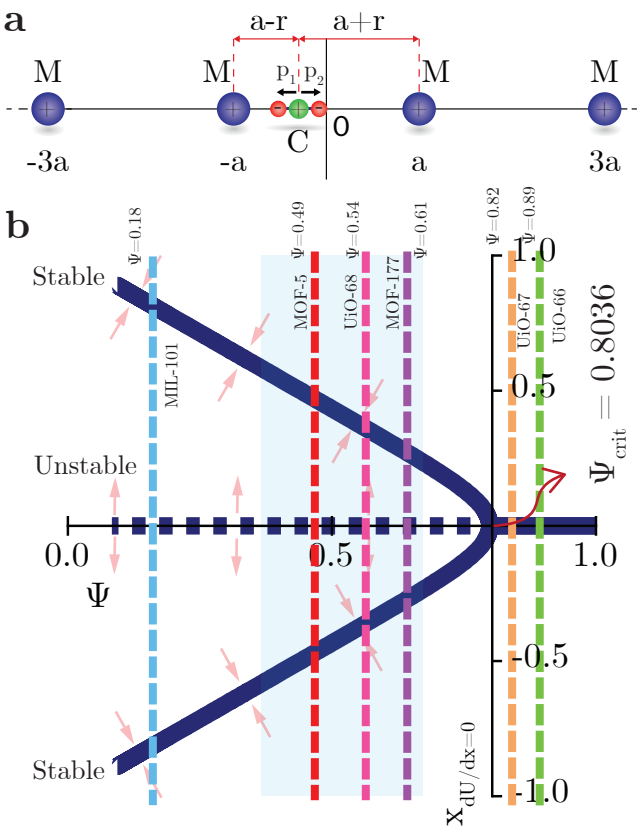

Fig. 8 One-dimensional model
a The *M* indicate the metal atoms separated by a distance $2a$, while *C* is the CO_2 molecule adsorbed at a distance r from the origin. $\vec{p}_1$ and $\vec{p}_2$ are the two opposing dipole moments forming a quadrupole. b Pitchfork bifurcation occurring at $\Psi = 0.8036$. For $\Psi > 0.8036$ only one stable equilibrium position exists inside the potential well. For $0 < \Psi < 0.8036$ two stable and one unstable equilibria are created. The vertical blue, purple, and green dotted lines denote positions of the MIL-101 ($\Psi = 0.18$), MOF-177 ($\Psi = 0.61$), and UiO-66 ($\Psi = 0.89$) on the bifurcation diagram, respectively.

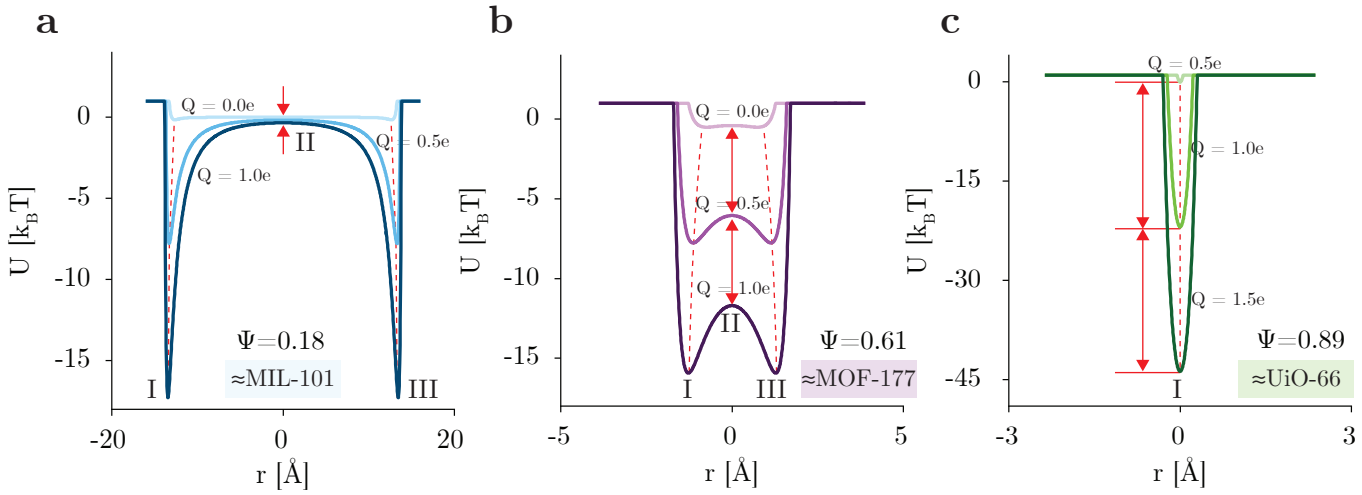

Fig. 9 Potential Wells

Schematic of the potential wells due to the van der Waals interactions in the one-dimensional MOF pores. In the case of a MIL-101 ($\Psi = 0.18$), the local minima (stable equilibrium) are close to the central metal atom (Cr) at positions I and III. The local maximum is at the center of the pore (unstable equilibrium) at position II. Similarly, in the case of MOF-177 ($\Psi = 0.61$), b the local minima (stable equilibrium) are close to the central metal atom (Zn) at positions I and III, and the local maximum is at the center of the pore (unstable equilibrium) at position II. In the case of UiO-66 ($\Psi = 0.89$), c the potential has only one minimum (stable equilibrium). The darker shade represents a higher charge on the central metal atom (Q). The equilibrium positions shift less than 15% of the unit cell length.

in Eq. 5 can be written as,

$$x(x^2 - \tilde{c})P(x^{18}) = 0,$$

$$\text{here,} \quad \tilde{c} = f(\Psi, Q, \mu, \varepsilon_{mc}) \tag{6}$$

Here, $\tilde{c}$ is a function of $\Psi, Q, \mu, \varepsilon_{mc}$ and $P(x^{18})$ is a 18-degree polynomial. The Matlab code for the one-dimensional model is attached to the electronic version of this manuscript[1].

Eq. 6 is the normal form of the pitchfork bifurcation with[54]

$$\frac{\partial \tilde{U}}{\partial x} = \tilde{c}x - x^3 \tag{7}$$

For Eq. 6 to have real roots other than $x = 0$, $\tilde{c}$ must be > 0. Therefore, for $Q = 0.5e$, $\varepsilon_m = 65$ [K], and $\sigma_m = 2.5$ [Å], $\Psi_{crit} = 0.8036$. This implies that when Ψ is in the range $(0, 0.8036)$, there are two stable and one unstable equilibrium. For Ψ in the range $[0.8036, 1)$, there is only one stable equilibrium, as shown in Fig. 8**b**. Therefore, we define a critical value of the confinement parameter as $\Psi_{\text{crit}} = 0.8036$.

Plotting the roots of $\frac{\partial \tilde{U}}{\partial x} = 0$ in Eq. 7 $(0, \pm\sqrt{\tilde{c}})$ with respect to x gives the curve for the supercritical pitchfork bifurcation, as shown in Fig. 8**b**. Plotting Eq. 4 for the metal atoms and CO_2 adsorbate for MIL-101 (Cr) gives $\Psi = 0.18$ potenial wells, while MOF-177 (Zn) gives $\Psi = 0.61$ and UiO-66 (Zr) gives $\Psi = 0.89$ potential wells, as shown in Fig. 9. Here, the depth of the potential wells depends on the parameter ε_{mc} in Eq. 3, which determines ΔH_{ads} at lower N/N_{max}. For UiO-66, the metal atoms at $(\pm 3a, 0)$ contribute to the depth of the potential well up to 23% of the total value. On the other hand, for MOF-177 and MIL-101, this contribution falls to around 0.3% and 0.0007%, respectively. This supports the hypothesis that for UiO-66, the greater ΔH_{ads} is due to interactions with metal atoms beyond the unit cell of adsorption.

The MIL-101 has the lowest potential (adsorption site) near the Cr-metal site (Fig. 9**a**), which is seen from the RDFs (Fig. 7**a**). Thus, the smallest pore fills up first. As the pressure increases, the medium and large cavities are filled, which is evident from the adsorption isotherm (Fig. 4**a**), differential enthalpy of adsorption (Fig. 5**a**), and the pore-filling process in the ESI[1] (Fig. S16).

The MOF-177 (Fig. 9**b**) has only one pore, and the depth of the potential well is skewed slightly toward the metal atoms; hence, pore filling at lower pressures is near the Zn-metal site. As Ψ is close to Ψ_{crit}, even at moderate pressure levels, the pore fills up uniformly. This leads to capillary condensation at a much lower relative pressure, as seen in the previous sections (grey shaded region in Fig. 5**b**). In the case of UiO-66 (Fig. 9**c**), $\Psi > \Psi_{\text{crit}}$, which implies there is only one stable equilibrium position at the pore center. Thus, the adsorption site must be at the center of the pore, which is affirmed by the RDFs in Fig. 7**e**.

It is crucial to acknowledge that the applicability of the one-dimensional model discussed earlier may have limitations, particularly in cases where multiple metal sites are present within the MOF structure. An example is PCN-221 (see Sec. S5), where the confinement parameter $\Psi = 0.91$ suggests a Type I adsorption isotherm; however, GCMC simulations reveal a step in the adsorption isotherm instead. This mismatch in trend can be attributed to the presence of multiple metal sites within the framework of PCN-221 (Cu and Zr), indicating the need for further investigation to understand the underlying mechanisms and factors responsible for this behavior.

5 Conclusion

Three MOFs with varying pore sizes illustrate the effects of the degree of confinement on the adsorption isotherm shape as well

as the heat of adsorption. Optimizing the amount of CO_2 adsorbed and the differential enthalpy of adsorption maximizes the total heat released with respect to pressure. This work qualitatively analyzes the effects of pore diameter on the heat of adsorption. The adsorption isotherms and heat of adsorption for CO_2 in MIL-101, MOF-177, and UiO-66 were measured experimentally. The GCMC simulations help understand the pore-filling mechanism and attain a general concept of the CO_2 molecule packing in the adsorbed states. Moreover, a simple one-dimensional model provides the confinement parameter (Ψ), the ratio of the L–J parameter σ_{ma}, and the pore radius. Bulk behavior is observed for values of Ψ tending to 0. For $\Psi \in (0, \Psi_{crit})$, there exists a double potential well with two stable equilibria and one unstable equilibrium (MIL-101 and MOF-177). For MOF-177, Ψ is larger than MIL-101 and still lower than Ψ_{crit}. Therefore, capillary condensation occurs at low pressures ($P/P_{sat} \approx 0.1$). For $\Psi > \Psi_{crit}$, there is a single well with one stable equilibrium (UiO-66). Due to volumetric constraints, only monolayer adsorption can occur, preventing the possibility of capillary condensation.

In a previous study,[8] we proposed the concept of an HCA-HP cycle based on the sorption of CO_2 in MOFs. To achieve maximum performance from such a cycle, the adsorbent (MOF) (i) must have a high heat of adsorption (enthalpy of phase change on the order of $\sim$ 10–100 kJ/mol) to maximize the output, and (ii) must have a step-shaped adsorption-desorption isotherm to reduce the work required for regeneration by creating a low operating pressure ratio. The present study focuses on investigating the influence of pore size on the adsorption process. By considering the adsorption of particles as being confined within potential wells of varying depths, the equilibrium properties of these particles can be correlated with the shape of the potential well. A one-dimensional model is employed to examine the behavior of these wells, revealing a distinct bifurcation in their shapes in relation to the confinement parameter Ψ. Notably, within the range of Ψ values between 0.4 and 0.6, a stepwise adsorption isotherm is observed at relatively low pressures, as demonstrated in the case of MOF-177, MOF-5, and UiO-68 in this particular study. Consequently, the optimal cumulative enthalpy of adsorption for heat pump applications can be achieved by designing MOFs with Ψ values falling within this range.

Author Contributions

Gunjan Auti: conceptualization, simulation, experiments, data acquisition, validation, numerical modeling, visualization, writing original draft, reviewing, and editing. Yuki Kametani: sample synthesis and validation, writing, reviewing, and editing. Hibiki Kimura: simulation, data acquisition, writing, reviewing, and editing. Soumyadeep Paul: numerical modeling, writing, reviewing, and editing. Wei-Lun Hsu: writing, reviewing, and editing. Shinpei Kusaka: experiments, writing, reviewing, and editing. Ryotaro Matsuda: experiments, writing, reviewing, and editing. Takashi Uemura: writing, reviewing, and editing. Shohei Chiashi: writing, reviewing, and editing. Hirofumi Daiguji: conceptualization, writing, reviewing, editing, supervision, and funding acquisition.

Conflicts of interest

There are no conflicts to declare.

Acknowledgements

This work was supported by JST, CREST Grant Number JPMJCR17I3, Japan.

Notes and references

1 See Supplemental Material at [URL will be inserted by publisher] for further information.
2 J. W. Baldwin, J. B. Dessy, G. A. Vecchi and M. Oppenheimer, *Earth's Future*, 2019, **7**, 411–427.
3 T. C. Peterson, P. A. Stott and S. Herring, *Bulletin of the American Meteorological Society*, 2012, **93**, 1041–1067.
4 International Energy Agency, *The Future of Cooling*, https://www.iea.org/reports/the-future-of-cooling, 2018, License: CC BY 4.0.
5 *Montreal Protocol*, https://www.unido.org/, Accessed: 2022-08-18.
6 *EPA*, https://www.epa.gov/, Accessed: 2022-08-18.
7 M. O. McLinden, J. S. Brown, R. Brignoli, A. F. Kazakov and P. A. Domanski, *Nature Communications*, 2017, **8**, 1–9.
8 J. A. Shamim, G. Auti, H. Kimura, S. Fei, W.-L. Hsu, H. Daiguji and A. Majumdar, *Cell Reports Physical Science*, 2022, **3**, 101131.
9 C. Wang, D. Liu and W. Lin, *Journal of the American Chemical Society*, 2013, **135**, 13222–13234.
10 S. K. Henninger, H. A. Habib and C. Janiak, *Journal of the American Chemical Society*, 2009, **131**, 2776–2777.
11 W. Li, X. Xia and S. Li, *Journal of Materials Chemistry A*, 2019, **7**, 25010–25019.
12 A. J. Rieth, A. M. Wright, S. Rao, H. Kim, A. D. LaPotin, E. N. Wang and M. Dinca, *Journal of the American Chemical Society*, 2018, **140**, 17591–17596.
13 M. F. de Lange, K. J. Verouden, T. J. Vlugt, J. Gascon and F. Kapteijn, *Chemical reviews*, 2015, **115**, 12205–12250.
14 F. Schüth, K. S. W. Sing and J. Weitkamp, *Handbook of porous solids*, Wiley-Vch, 2002.
15 H. Li, K. Wang, Y. Sun, C. T. Lollar, J. Li and H.-C. Zhou, *Materials Today*, 2018, **21**, 108–121.
16 H. Daglar, H. C. Gulbalkan, G. Avci, G. O. Aksu, O. F. Altundal, C. Altintas, I. Erucar and S. Keskin, *Angewandte Chemie International Edition*, 2021, **60**, 7828–7837.
17 Y.-S. Bae and R. Q. Snurr, *Angewandte Chemie International Edition*, 2011, **50**, 11586–11596.
18 A. L. Dzubak, L.-C. Lin, J. Kim, J. A. Swisher, R. Poloni, S. N. Maximoff, B. Smit and L. Gagliardi, *Nature chemistry*, 2012, **4**, 810–816.
19 A. I. Cooper, *Nature*, 2015, **519**, 294–295.
20 A. Agrawal, M. Agrawal, D. Suh, Y. Ma, R. Matsuda, A. Endo, W.-L. Hsu and H. Daiguji, *Journal of Materials Chemistry A*, 2020, **8**, 16385–16391.
21 J. S. Seo, D. Whang, H. Lee, S. I. Jun, J. Oh, Y. J. Jeon and K. Kim, *Nature*, 2000, **404**, 982–986.

22 B. N. Bhadra, A. Vinu, C. Serre and S. H. Jhung, *Materials Today*, 2019, **25**, 88–111.

23 P. Horcajada, T. Chalati, C. Serre, B. Gillet, C. Sebrie, T. Baati, J. F. Eubank, D. Heurtaux, P. Clayette, C. Kreuz *et al.*, *Nature materials*, 2010, **9**, 172–178.

24 J. M. Goncalves, P. R. Martins, D. P. Rocha, T. A. Matias, M. S. Juliao, R. A. Munoz and L. Angnes, *Journal of Materials Chemistry C*, 2021, **9**, 8718–8745.

25 P. G. Youssef, H. Dakkama, S. M. Mahmoud and R. K. AL-Dadah, *Desalination*, 2017, **404**, 192–199.

26 T. C. Wang, W. Bury, D. A. Gómez-Gualdrón, N. A. Vermeulen, J. E. Mondloch, P. Deria, K. Zhang, P. Z. Moghadam, A. A. Sarjeant, R. Q. Snurr *et al.*, *Journal of the American Chemical Society*, 2015, **137**, 3585–3591.

27 R. Grünker, V. Bon, P. Müller, U. Stoeck, S. Krause, U. Mueller, I. Senkovska and S. Kaskel, *Chemical Communications*, 2014, **50**, 3450–3452.

28 G. K. Papadopoulos, *The Journal of Chemical Physics*, 2001, **114**, 8139–8144.

29 T. A. Steriotis, K. Stefanopoulos, N. Kanellopoulos, A. C. Mitropoulos and A. Hoser, *Colloids and Surfaces A: Physicochemical and Engineering Aspects*, 2004, **241**, 239–244.

30 Y. B. Melnichenko, H. Mayama, G. Cheng and T. Blach, *Langmuir*, 2010, **26**, 6374–6379.

31 I. Gimondi and M. Salvalaglio, *Molecular Systems Design & Engineering*, 2018, **3**, 243–252.

32 G. Rother, E. G. Krukowski, D. Wallacher, N. Grimm, R. J. Bodnar and D. R. Cole, *The Journal of Physical Chemistry C*, 2012, **116**, 917–922.

33 T. Sanghi and N. Aluru, *The Journal of chemical physics*, 2012, **136**, 024102.

34 M. D. Elola and J. Rodriguez, *The Journal of Physical Chemistry C*, 2016, **120**, 1262–1269.

35 G. Férey, C. Mellot-Draznieks, C. Serre, F. Millange, J. Dutour, S. Surblé and I. Margiolaki, *Science*, 2005, **309**, 2040–2042.

36 H. K. Chae, D. Y. Siberio-Pérez, J. Kim, Y. Go, M. Eddaoudi, A. J. Matzger, M. O'Keeffe, O. M. Yaghi, M. Design and D. Group, *Nature*, 2004, **427**, 523–527.

37 A. Schaate, P. Roy, A. Godt, J. Lippke, F. Waltz, M. Wiebcke and P. Behrens, *Chemistry–A European Journal*, 2011, **17**, 6643–6651.

38 S. Brunauer, P. H. Emmett and E. Teller, *Journal of the American chemical society*, 1938, **60**, 309–319.

39 D. Y. Siberio-Pérez, A. G. Wong-Foy, O. M. Yaghi and A. J. Matzger, *Chemistry of materials*, 2007, **19**, 3681–3685.

40 D. Dubbeldam, S. Calero, D. E. Ellis and R. Q. Snurr, *Molecular Simulation*, 2016, **42**, 81–101.

41 J. J. Potoff and J. I. Siepmann, *AIChE journal*, 2001, **47**, 1676–1682.

42 G. Perez-Sanchez, D. González-Salgado, M. Pineiro and C. Vega, *The Journal of Chemical Physics*, 2013, **138**, 084506.

43 A. K. Rappé, C. J. Casewit, K. Colwell, W. A. Goddard III and W. M. Skiff, *Journal of the American chemical society*, 1992, **114**, 10024–10035.

44 C. E. Wilmer, K. C. Kim and R. Q. Snurr, *The journal of physical chemistry letters*, 2012, **3**, 2506–2511.

45 G. B. Woods, A. Z. Panagiotopoulos and J. S. Rowlinson, *Molecular Physics*, 1988, **63**, 49–63.

46 B. Smit and J. I. Siepmann, *The Journal of Physical Chemistry*, 1994, **98**, 8442–8452.

47 T. Vlugt, E. García-Pérez, D. Dubbeldam, S. Ban and S. Calero, *Journal of Chemical Theory and Computation*, 2008, **4**, 1107–1118.

48 D. Cao and S. Sircar, *Adsorption Science & Technology*, 2001, **19**, 887–894.

49 R. Zsigmondy, *Zeitschrift für anorganische Chemie*, 1911, **71**, 356–377.

50 S. Gregg and K. Sing, *Academic Press, London*, 1982, **3**, 195–247.

51 T. Watanabe and D. S. Sholl, *Langmuir*, 2012, **28**, 14114–14128.

52 D. Liu, C. Zheng, Q. Yang and C. Zhong, *The Journal of Physical Chemistry C*, 2009, **113**, 5004–5009.

53 B. M. Mognetti, L. Yelash, P. Virnau, W. Paul, K. Binder, M. Müller and L. G. MacDowell, *The Journal of chemical physics*, 2008, **128**, year.

54 S. H. Strogatz, *Nonlinear dynamics and chaos: with applications to physics, biology, chemistry, and engineering*, CRC press, 2018.